ACS MATERIALS Au
AN OPEN ACCESS JOURNAL OF THE AMERICAN CHEMICAL SOCIETY

pubs.acs.org/materialsau Article

Structure–Processing–Property Relationships of 3D Printed Porous Polymeric Materials

Ciera E. Cipriani, Taekwang Ha, Oliver B. Martinez Defilló, Manoj Myneni, Yifei Wang, Chandler C. Benjamin, Jyhwen Wang,* Emily B. Pentzer,* and Peiran Wei*

Cite This: *ACS Mater. Au* 2021, 1, 69–80 Read Online

ACCESS | Metrics & More | Article Recommendations | Supporting Information

ABSTRACT: Imparting porosity to 3D printed polymeric materials is an attractive option for producing lightweight, flexible, customizable objects such as sensors and garments. Although methods currently exist to introduce pores into 3D printed objects, little work has explored the structure–processing–property relationships of these materials. In this study, photopolymer/sacrificial paraffin filler composite inks were produced and printed by a direct ink writing (DIW) technique that leveraged paraffin particles as sacrificial viscosity modifiers in a matrix of commercial elastomer photocurable resin. After printing, paraffin was dissolved by immersion of the cured part in an organic solvent at elevated temperature, leaving behind a porous matrix. Rheometry experiments demonstrated that composites with between 40 and 70 wt % paraffin particles were able to be successfully 3D printed; thus, the porosity of printed objects can be varied from 43 to 73 vol %. Scanning electron microscopy images demonstrated that closed-cell porous structures formed at low porosity values, whereas open-cell structures formed at and above approximately 53 vol % porosity. Tensile tests revealed a decrease in elastic modulus as the porosity of the material was increased. These tests were simulated using finite element analysis (FEA), and it was found that the Neo-Hookean model was appropriate to represent the 3D printed porous material at lower and higher void fractions within a 75% strain, and the Ogden model also gave good predictions of porous material performance. The transition between closed- and open-cell behaviors occurred at 52.4 vol % porosity in the cubic representative volume elements used for FEA, which agreed with experimental findings that this transition occurred at approximately 53 vol % porosity. This work demonstrates that the tandem use of rheometry, FEA, and DIW enables the design of complex, tailorable 3D printed porous structures with desired mechanical performance.

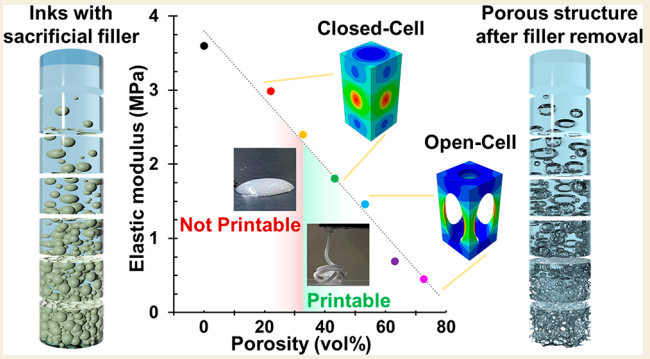

KEYWORDS: *3D printing, direct ink writing, porous material, open-cell foam, closed-cell foam, finite element analysis*

INTRODUCTION

Porosity is a property that offers a variety of benefits within polymer-based structures, including high surface area-to-volume ratio, flexibility, and selective permeability.[1] Thus, porous materials have broad applications in adsorption,[2,3] separation,[4−6] sensing,[7,8] catalysis,[9,10] and biomedical engineering.[11−13] Combining porosity with advanced manufacturing methods such as 3D printing (3DP) is an attractive option for producing objects with complex geometries, such as custom shoe midsoles,[14,15] football helmet linings,[16] battery electrodes,[17] tissue scaffolds,[11,13,18] and biomimicking materials.[19−21] Despite these benefits, further developments are required for porous polymeric materials to realize their full potential within 3DP.

Among different 3DP techniques, direct ink writing (DIW) has become popular as a result of its low cost, ease of use, and ability to tailor ink composition.[22] DIW inks must be thixotropic so that they are shear-thinning and highly viscous to hold their shape after extrusion.[22,23] DIW printers are able to print many different ink compositions, including colloidal gels/suspensions,[24−26] polymers,[27] ceramics,[28,29] and nanoparticles.[17,30] The concentration of particle additives influences the viscosity and shear-thinning behavior of a 3D printing ink.[8,31,32] These particle additives are commonly removed to produce porous 3D printed structures.[8,31,33] In such systems, the porosity of a 3D printed porous material is directly dependent on the concentration of viscosity modifying particle additives. This relationship between rheological performance, porosity, and mechanical properties has not previously been

Received: May 21, 2021
Published: July 23, 2021

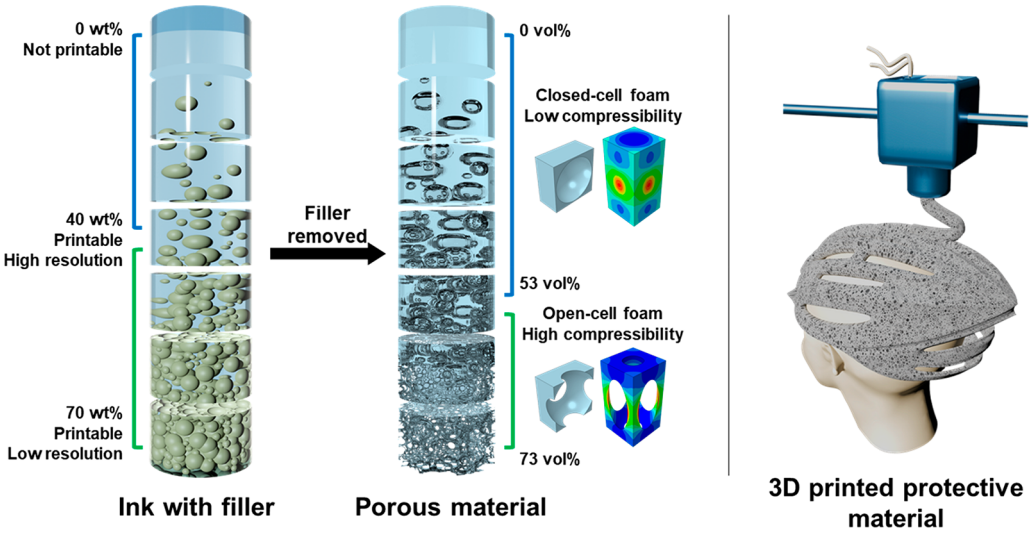

Figure 1. Schematic illustrating the preparation of the thixotropic ink composed of paraffin wax beads and photopolymerizable resin, removal of filler resulting in closed- or open-cell structures of the printed porous materials, representative volume elements used for FEA, and potential application for 3D printed protective materials. Increasing paraffin loading, as shown from top to bottom in the ink on the left, results in increased porosity in the porous material and thus tunable mechanical performance.

explored. A deeper understanding of the particle loading, internal structure, and mechanical performance would facilitate the development of printable inks for DIW with desired properties in the resulting printed porous material.

To produce porous materials and leverage the distinct opportunities of 3DP, appropriate feedstock compositions must be realized. Current techniques for 3DP porous polymeric materials include printing lattice structures in which porosity is imparted by the print path,[11,31] particle-stabilized nanoemulsions based on sacrificial templates,[34] polymer matrices with sacrificial fillers,[8,31,33] polymer solutions with pores formed by solvent evaporation,[35] and polymers with intrinsic porosity.[36] Each of these approaches imparts porosity on a different size scale and can be combined to produce hierarchically porous structures.[18] Printing porous lattice structures gives control over porosity at the scale of the print resolution (usually micrometers or larger). The porosity imparted by the print path is highly controllable, but the pore size is limited by the resolution of the printer, which restricts the geometric detail that can be achieved from these porous prints. Porosity resulting from sacrificial templates and fillers depends on the filler size (generally on the nanometer to micrometer scale) and often requires harsh conditions, such as extreme temperatures[8,37] or corrosive chemicals,[8,31] to remove the sacrificial material. It is possible to use sacrificial templates without harsh conditions, as exemplified by Magdassi et al., who developed photopolymerizable oil-in-water emulsions that contained monomers in the dispersed phase which formed a porous polymeric material upon ultraviolet light curing and removal of water.[34] Similarly, Qi et al. used salt as a sacrificial filler which was removed by soaking in water.[33] In contrast, the Wegener group has harnessed polymerization-induced phase separation to 3D print inherently nanoporous structures using both digital light processing 3DP and 3D laser microprinting techniques.[36,38] Printing polymers with intrinsic porosity offers molecular-scale pores formed by voids between polymer chains, but the size and distribution of the pores are less easily controlled than larger-scale methods. Using polymers with intrinsic porosity also limits the materials which are accessible for 3DP of porous structures. To develop 3D printed porous materials with the desired properties, multiple techniques can be combined to produce hierarchically porous structures. For example, Zhang and coauthors created biocomposite scaffolds with macropores ranging between 100 and 800 μm in diameter which were formed by the print path, along with micropores ranging between 2 and 10 μm in diameter which were formed by gas foaming and solvent etching of sacrificial fillers.[18] 3DP offers unique control over the macrostructure of printed objects, and 3DP materials can be tailored to obtain desired microstructures. Although much progress has been made in the development of 3D printed porous polymeric materials, there is a need for a facile method for producing these materials, adjusting their porosity, and understanding the relationships between structure, processing, and properties to print structures with desired porosity and mechanical performance.

The structure−property relationships of porous materials are commonly described using a combination of imaging and finite element analysis (FEA). Imaging methods such as scanning electron microscopy,[39,40] tunneling electron microscopy,[40] and X-ray tomography[40,41] provide information about pore shape and distribution, which is used to develop models of porous materials for use in FEA. Compressive,[40] tensile,[39] and other mechanical tests can be simulated using FEA, and the results are commonly compared to experiments. In the present work, we describe a facile approach for 3DP porous materials which was paired with structure-processing-property characterization to predict printability, porosity, and mechanical performance. We hypothesized that the porosity of a 3DP structure could be tuned by using particles of solid paraffin wax as sacrificial rheological modifiers for a commercially available elastomer photopolymer resin, then removing the wax. We previously demonstrated that particles of different organic phase change materials could render such resins printable by DIW. The resulting structure is useful in thermal energy management and maintains performance even after exposure to harsh thermal and chemical conditions.[32] We hypothesized that after DIW printing and ultraviolet light curing, the spherical, micrometer-

https://doi.org/10.1021/acsmaterialsau.1c00017
ACS Mater. Au 2021, 1, 69−80

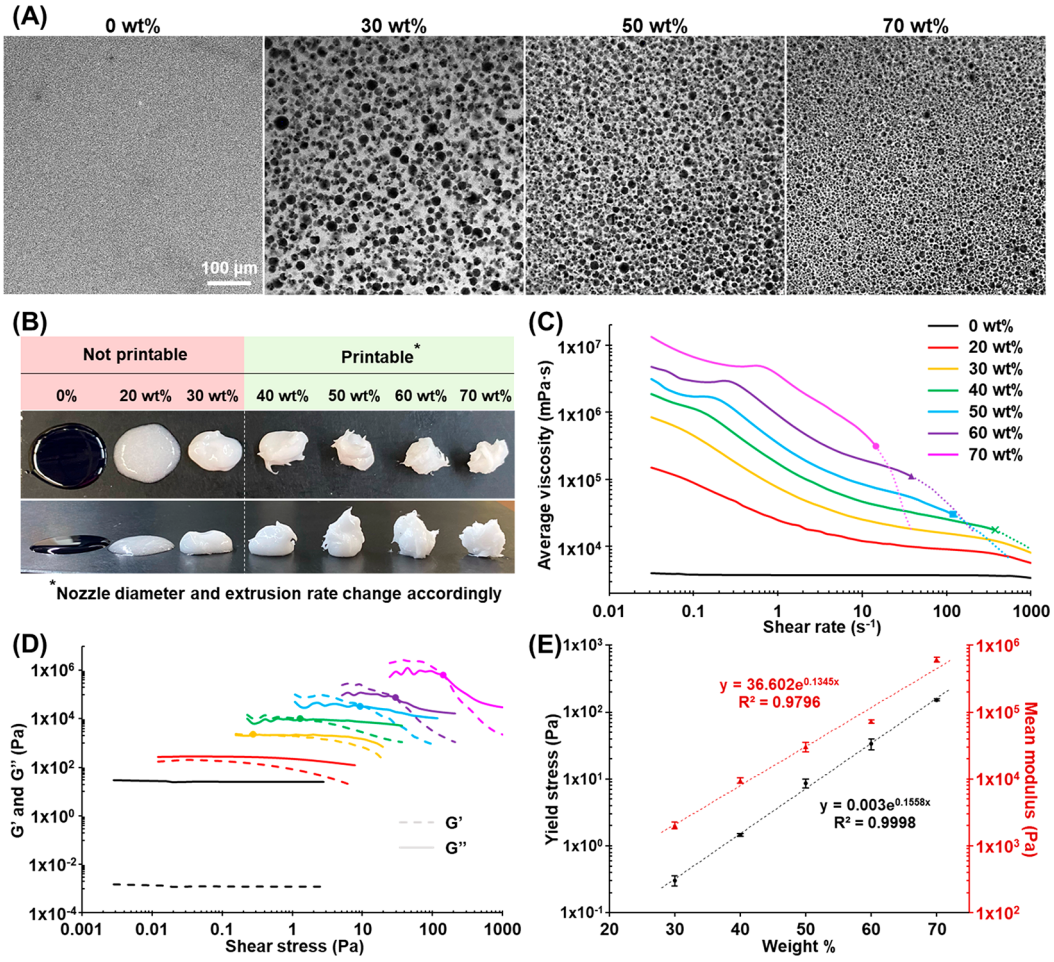

Figure 2. (A) Confocal microscopy images of resin and paraffin/photopolymer composite inks. (B) Printability classification and digital images of inks of varying wt % paraffin. (C) Average viscosity of each ink as a function of shear rate (dashed lines are regions where the ink was expelled from the sides of the parallel plate). (D) Storage modulus and loss modulus as a function of stress amplitude. (E) Mean yield stress and mean shear modulus at yield of each ink. Error bars indicate standard deviation (n = 3).

scale paraffin particles could be removed from the polymer/sacrificial filler composites through solvent extraction, leaving voids in the printed objects. The paraffin could then be recovered from the solvent, and both the paraffin and solvent could be reused. Inks with different paraffin loading levels could be combined by DIW to control the porosity of specific areas within printed objects, as illustrated in Figure 1. The present study focuses on the structure of this new feedstock for 3D printed porous materials and the resulting porous objects, the flow behavior and printability of the inks, and the mechanical properties of the porous materials. To this end, we have evaluated ink printability, rheological properties, and mechanical properties. Uniaxial tensile tests of the porous materials have been simulated using finite element analysis (FEA) to give insight into how the level of porosity influences the mechanical performance of these 3D printed porous photopolymers. It was found that inks with between 40 and 70 wt % paraffin were printable using DIW with different nozzle sizes based on ink viscosity. After printing and extraction of the paraffin, the porous materials with less than 53 vol % porosity had primarily closed-cell pores, whereas the porous materials with greater than 53 vol % porosity exhibited primarily open-cell characteristics.

RESULTS AND DISCUSSION

Inks for DIW must have appropriate rheological behavior to be printable; specifically, DIW inks should be thixotropic so that they are shear-thinning during extrusion, then quickly recover their high viscosity and thicken to maintain the shape of the printed object. In the present study, a printable ink is defined as having the ability to achieve a high-resolution object through the extrusion-based DIW technique. Generally, unmodified photocurable resins are not printable by DIW because they are Newtonian liquids, but micrometer- or nanometer-scale additives can impart non-Newtonian, thixotropic behavior.[8,31,32] In the present study, paraffin microbeads were selected as rheology modifiers. Beads of paraffin wax were prepared by emulsification at 80 °C in an aqueous solution of the surfactant Span 20 above the critical micelle concentration, then cooling to ambient temperature. Optical microscopy and scanning electron microscopy (SEM) images of the paraffin beads are shown in Figures S1 and S2, respectively. Figure S3 shows the size distribution histogram of the paraffin wax beads with an average diameter of 26 μm. These paraffin beads were incorporated into a commercial photocurable resin by hand mixing until a homogeneous ink was produced. The loading of the paraffin beads was varied based on the weight percent of wax in the resin, from 20 to 70 wt %. Confocal microscopy images of the resin itself and inks with 30, 50, and 70 wt %

https://doi.org/10.1021/acsmaterialsau.1c00017
ACS Mater. Au 2021, 1, 69−80

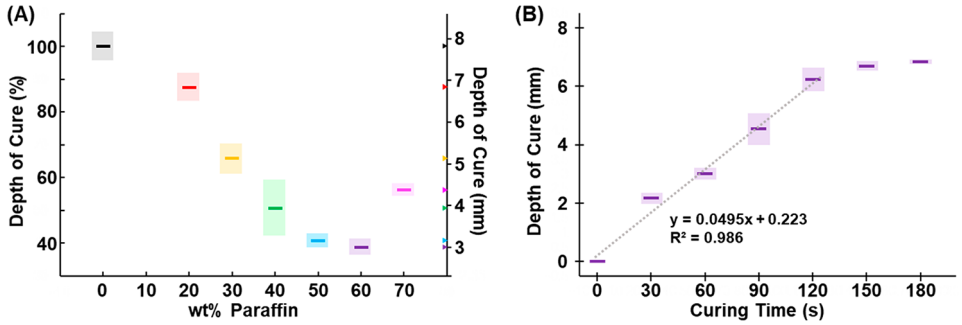

Figure 3. (A) The depth of cure of each ink after exposure to 365 nm light for 1 min. Error bars indicate standard deviation (n = 3). (B) The depth of cure of 60 wt % paraffin ink after exposure to 365 nm light for 30, 60, 90, 120, 150, or 180 s (n = 3).

paraffin are displayed in Figure 2A, and a comparison of all inks (20, 30, 40, 50, 60, and 70 wt % paraffin particles) is displayed in Figure S4. The dark regions in the confocal microscopy images correspond to the paraffin beads; as the paraffin loading increased, the number of beads observed increased. For all inks, the paraffin beads were spherical and dispersed in size. Visually, the degree of size dispersity was similar between all samples. Notably, increased paraffin loading caused the observed particle size to appear smaller, but the paraffin beads used in these samples were all prepared in the same batch. The apparent decrease in size of the paraffin beads with increasing loading is likely a result of decreased penetration depth of the light of the confocal microscope into the ink.

For all inks, the shear stress applied during their extrusion from a DIW printer must be greater than that at the yield point to induce a viscous flow of the ink. Thus, the rheological properties of ink can be used to predict DIW printability. The printability of inks with different loadings of paraffin beads was primarily evaluated by viscosity, yield stress, and mean storage/loss modulus. The increased viscosity with increasing paraffin loading was first observed by depositing the inks from a spatula onto a surface as shown in the digital images in Figure 2B. From visual inspection, it appeared that inks with less than 30 wt % paraffin could not hold their shape well enough to be extruded. As displayed in Figure 2C and Figure S5, the as-received photocurable resin was a Newtonian liquid, as expected, with a viscosity that was independent of shear rate (black trace). Incorporating paraffin beads into this resin imparted shear-thinning behavior, whereby the viscosity decreased as the shear rate increased. In general, increasing the filler concentration increased the measured viscosity. For example, at a shear rate of 1 s^{-1}, the viscosity of resin was 3700 mPa·s, and that of 70 wt % paraffin ink was 3.7 × 10^6 mPa·s. The magnitude of the shear-thinning behavior (i.e., the slope) near a shear rate of 1 s^{-1} decreased with increasing paraffin loading up to 30 wt %. The magnitude of the shear-thinning behavior was similar in the samples containing 40 to 70 wt % paraffin. Slight shear-thickening behavior was observed in the highly filled inks at shear rates below 1 Hz, which may result from transient yielding of these samples during testing. At high shear rates, samples with 40 wt % paraffin loading or greater were expelled from the sides of the parallel plates (Figure S6). The viscosity curves in Figure 2C are truncated at these points, and dashed lines indicate data that was collected after the expulsion of the ink. Full traces of the average viscosities of the inks are available in Figure S5. A sharp decline in the viscosity at high shear rates is clear in the traces of the 60 and 70 wt % paraffin inks, which corresponds to the expulsion of each ink from the sides of the parallel plates. In less highly filled inks, the decline in viscosity is less obvious. It is necessary to consider this phenomenon when performing rheological testing of filled materials.

Shear stress amplitude sweeps were performed at a frequency of 1 Hz to identify the yield stress (Figure 2D) and mean storage/loss modulus at the yield point (Figure 2E) of each ink. Although single values for the yield point are commonly reported, in reality, yielding is a gradual process and is not fully described by a single point.[42] Additionally, various methods of yield point determination exist, such as taking the point at which the storage modulus begins to deviate from linearity, the point at which the stress−strain response deviates from linearity, or the crossover point between the storage and loss moduli.[43] In the present study, yielding was described by a single point using the latter approach for simplicity. Although other methods may produce different yield point values, the trend of increasing yield point with increasing paraffin loading should hold. The resin and 20 wt % paraffin ink did not have yield points, which indicates they are simply viscous liquids. Polymer solutions often exhibit viscoelastic behavior as a result of polymer disentanglement during shear. In the present manuscript, the commercial unfilled resin comprises small molecules and oligomers; therefore, it only exhibits viscous characteristics regardless of shear rate. In contrast, the 30 to 70 wt % paraffin inks exhibited viscoelastic behavior, with the storage modulus, loss modulus, and yield stress increasing with increased paraffin loading. The elastic characteristics of the most highly filled inks can be attributed to interactions between paraffin particles, which form a weak solid structure and facilitate printing by DIW.[44] Optimized inks must have low enough viscosities to be extruded by a DIW printer with a specified nozzle size and also hold their shape after extrusion to achieve the desired shape of a printed object. For the reported composites, the variation in viscosity, shear-thinning behavior, yield stress, and yield modulus indicates that paraffin particle loading can be used to achieve optimal thixotropic behavior for DIW inks, since materials undergo shear during the extrusion process.

The depth of cure (DOC) of ink under a particular UV light source determines the maximum diameter of a printable filament and thus the printing resolution. To evaluate the effect of paraffin bead loading on the DOC of inks, we filled 2 mL scintillation vials with inks having different loading levels of paraffin, then cured them from the bottom using a 365 nm Hyrel UV Pen for different time intervals and measured the height of the ink that was cured. As the elasticity of cured

https://doi.org/10.1021/acsmaterialsau.1c00017
ACS Mater. Au 2021, 1, 69−80

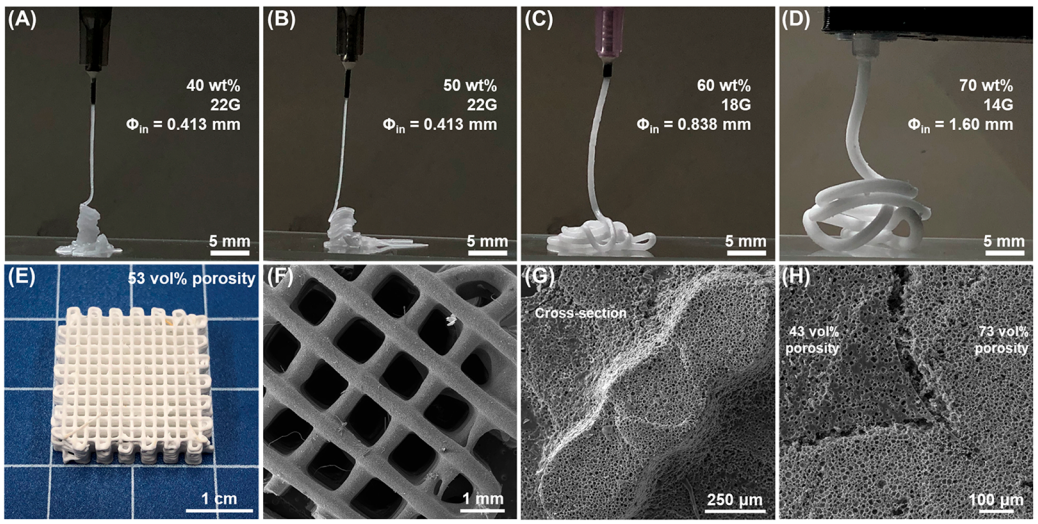

Figure 4. Digital images of DIW of (A) 40 wt % paraffin ink out of a 22G nozzle, (B) 50 wt % paraffin ink out of a 22G nozzle, (C) 60 wt % paraffin ink out of an 18G nozzle, and (D) 70 wt % paraffin ink out of a 14G nozzle. (E) Porous cubic lattice printed using 50 wt % paraffin ink (53 vol % porosity). (F) SEM image of cubic lattice printed with 53 vol % porosity. (G) SEM image of the cross-section of the cubic lattice printed with 53 vol % porosity, and (H) SEM image of the cross-section of the cubic lattice printed with 43 vol % and 73 vol % porosity adjacent to one another.

materials depends on the intensity of the light source,[45] samples were cured in a random order to mitigate the effect of drift in the light source intensity over time. Numerical measurements of the DOC for each ink are available in Table S1, and a digital image of representative cured samples is in Figure S7. As shown in Figure 3A, increasing filler content caused the DOC to gradually decrease which can be attributed to scattering and impeding of incoming light by the paraffin beads. Unexpectedly, the ink with 70 wt % paraffin had a higher DOC than the 40, 50, and 60 wt % paraffin inks. The cause of this anomaly is unknown, and future work may probe other paraffin concentrations to determine the full trend relating paraffin loading to DOC. The dependence of the DOC on curing time was also examined by irradiating vials of 60 wt % paraffin ink for 30, 60, 90, 120, 150, or 180 s and measuring the DOC of each sample. From the plot in Figure 3B (numerical data available in Table S2), we found a positive linear relationship between the sample curing time and DOC for UV exposure times of 120 s or less. Above 120 s, the DOC value plateaued with a maximum measured DOC of 7.00 mm.

Alongside rheological results and depth of cure studies, printing resolution was evaluated using extrusion of liquid inks from a syringe. Nozzles with different gauges were used to identify the ideal inner diameter, Φ_{in}, for printing, as shown in Figure 4. Inks with less than 40 wt % paraffin did not possess optimal thixotropic behavior and flowed after extrusion; thus, these inks could not be 3D printed and were not evaluated for print resolution. As displayed in Figure 4A and 4B, the inks with 40 and 50 wt % paraffin were identified as printable by DIW because they had low enough viscosities to be extruded and thixotropic behavior to maintain their shape after extrusion using a 22G (Φ_{in} = 0.413 mm) nozzle. Similarly, the inks with 60 and 70 wt % paraffin were printable using 18G (Φ_{in} = 0.838 mm) and 14G (Φ_{in} = 1.60 mm) nozzles, respectively (Figure 4C,D). A digital image of the 60 wt % paraffin ink being printed is available in Figure S8, and Figure S9 shows printed cubic lattices of the 50, 60, and 70 wt % paraffin inks to demonstrate the increased filament size and decreased resolution of inks with higher loading of paraffin.

By relating the rheological data to these observational results, a range of printable yield stresses and moduli was found. Inks with yield stresses between 1.45 and 33.75 Pa, or with shear moduli at the yield point between approximately 10 000 and 100 000 Pa should be printable by DIW with a 22G and an 18G nozzle (due to the printability of inks with between 40 and 60 wt % paraffin). With the use of a larger 14G nozzle, the ink with 70 wt % paraffin was printable. Thus, the range of printability can be expanded to include materials with yield stresses up to approximately 150 Pa and yield points up to approximately 615 000 Pa by increasing the nozzle diameter. Higher paraffin loading sacrifices resolution based on the suitable gauge of the needle. Additional considerations when using highly loaded inks include having an adequate DOC to successfully cure printed filaments, along with ensuring that the motor of the printer is not overworked due to the force required for extrusion of highly viscous materials.

After producing the paraffin/photopolymer composites and curing them with ultraviolet light, the paraffin was removed by extraction with ethyl acetate at 80 °C and the samples were freeze-dried, resulting in pores within the photopolymer in place of the paraffin beads. Digital images of the cubic lattices before and after paraffin extraction in Figures S9 and S10 show that the printed objects did not deform or change resolution when the paraffin was removed. Complete paraffin removal was confirmed by measuring the mass loss of samples of cured ink containing 60 wt % paraffin, and these data are available in Table S3 and Figure S11. The experimental porosity was found to be comparable to the theoretical porosity. On the basis of the weight percentage of paraffin in each ink, the vol % porosities of the resulting porous structures were calculated and are reported in Table S4. Confocal microscopy (Figure S12) and SEM images (Figures S13−15) of the porous materials demonstrate that increased paraffin bead loading in the composite material led to increased porosity, and the size of the pores was found to be similar to the sizes of the paraffin beads given in Figure S3. Porosity was also maintained after printing; Figure 4E displays a printed cubic lattice with 53 vol % porosity, and SEM images of the lattice show pores on the micrometer scale (Figures 4F,G). Inks with different paraffin

https://doi.org/10.1021/acsmaterialsau.1c00017
ACS Mater. Au 2021, 1, 69−80

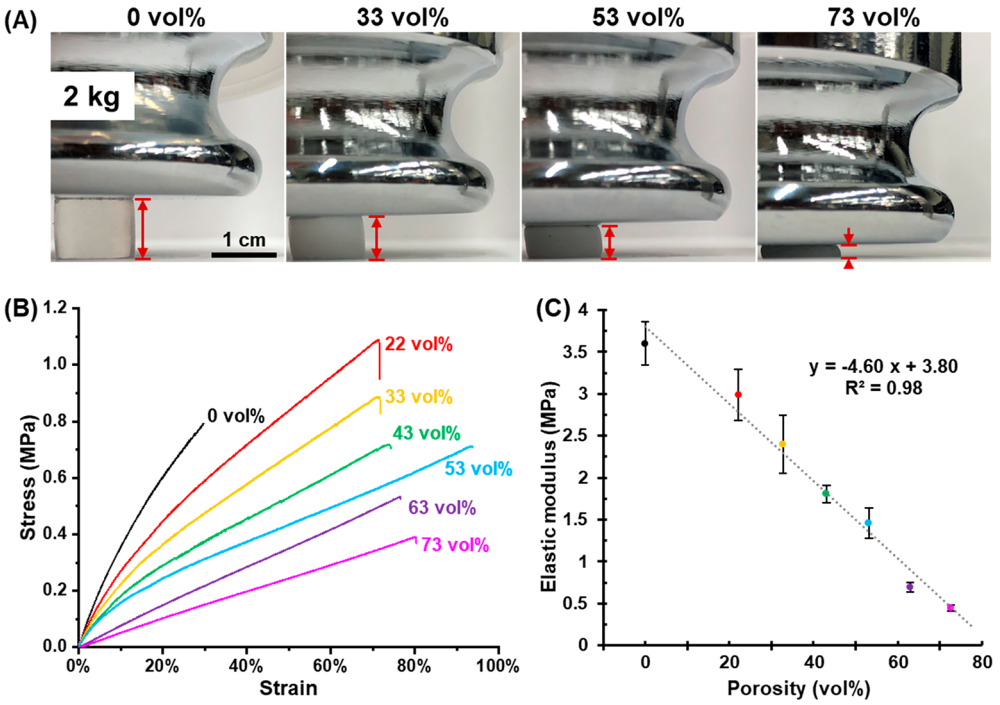

Figure 5. (A) Digital images of cylinders of varying porosity levels compressed by a 2 kg weight. (B) Representative experimental stress−strain curves resulting from tensile tests of materials with varying vol % porosity. (C) Experimental tensile modulus of samples with increasing porosity. Error bars indicate standard deviation (n = 5).

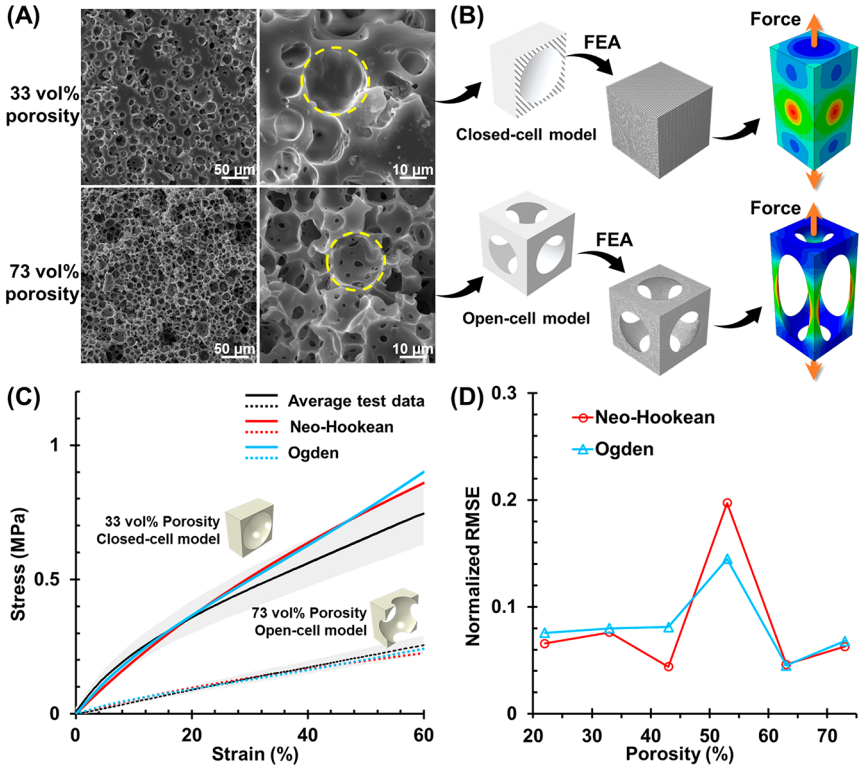

Figure 6. (A) SEM images of samples with 33 and 73 vol % porosity. (B) Illustration of a porous material and FE analysis with representative closed- and open-cell RVEs. (C) Stress−strain curves of ASTM D412 Type C samples with 33 vol % and 73 vol % porosity. Solid lines are experimental results, and dashed lines are FEA results, with the unit cells shown by the respective curves. (D) Normalized RMSE of the Neo-Hookean and Ogden models at different porosity levels.

loading levels can be printed next to one another to produce regions of different porosities as demonstrated in Figure 4H. Thus, paraffin/photopolymer composites can be used to produce 3D printed porous objects with complex geometries, and different levels of porosity can be incorporated into the same object.

https://doi.org/10.1021/acsmaterialsau.1c00017
ACS Mater. Au 2021, 1, 69−80

To evaluate the effects of increasing porosity on the compressibility of the photopolymer resin and porous materials, cylinders at each porosity level were compressed under a 2 kg weight, as shown in Figure 5A and Figure S16. As expected, increased porosity led to the sample being more compressed by the weight, indicating that the compressibility of these porous materials can be tuned by controlling the amount of paraffin loaded into the ink. Further, materials of varying porosity levels can be combined within one structure by tandem printing of different ink formulations to achieve regions of differing compressibility.

Samples with between 0 and 73 vol % porosity were prepared for tensile testing according to ASTM D612 Type C specifications, and the samples were tested on a Universal Testing System with a 1 kN load cell at a displacement rate of 20 mm/min. Representative stress−strain curves from one sample of each porosity are displayed in Figure 5B. Samples with 0 to 43 vol % porosity initially exhibited linear elastic deformation with nonlinear deformation occurring as the strain increased, whereas samples with 63 and 73 vol % porosity exhibited primarily linear elastic deformation up to fracture. In general, the samples with 53 vol % porosity exhibited higher extensibility than all of the other samples and had slight upward curvature at high strain. Average tensile moduli for five samples of each porosity are displayed in Figure 5C. Increased porosity resulted in a lower elastic modulus, as expected based on the increased flexibility of the samples.

To explain the characteristics of the porous samples that were observed in the tensile data, SEM images of the fractured surfaces of the tensile bars were taken. Representative images of the samples with 33 and 73 vol % porosity are displayed in Figure 6A. These images reveal that the pore density increased with increased paraffin loading, resulting in higher porosity, as expected. These images also provide insight into the microstructures of these porous materials. The sample with 33 vol % porosity contained primarily closed-cell pores, in which each pore was completely enclosed with polymer, and thus the pores were isolated from one another. In contrast, the 73 vol % porosity sample contained a high proportion of open-cell pores, in which windows connected pores to one another. This trend is exemplified by the SEM images of each porosity level from 22 to 73 vol % provided in Figure S17. Thus, we hypothesize that the different mechanical performance of the porous materials can be attributed to the change from a primarily closed-cell microstructure at low porosity to a primarily open-cell microstructure at high porosity.

To verify the hypothesis that the closed-to-open-cell transition of samples with different vol % porosity influences the mechanical performance, the tensile tests were simulated using finite element analysis (FEA). Several types of strain energy functions, including Neo-Hookean,[46] Mooney-Rivlin,[46,47] Ogden,[48] Yeoh,[49] and others, exist to predict nonlinear elastic material behavior. Assuming that this 3D printed porous material was incompressible and isotropic, we adopted two hyperelastic material models, the Neo-Hookean and Ogden, based on material parameters validated by experimentation.

To simulate uniaxial tensile testing of a porous material using FEA, the experimental stress−strain data of the bulk material without voids was input. From this, a tensile test of a sample of bulk cured resin (Figure S18) was approximated by both the Neo-Hookean and Ogden models, and the parameters for each model were determined and applied to simulated porous materials. For a material under uniaxial tension, the strain energy density and nominal stress predicted by the Neo-Hookean model are expressed with the uniaxial stretch ratio and given by the strain energy density function W:

$$W(\lambda_1) = c_1(\lambda_1^2 + 2\lambda_1^{-1} - 3) \tag{1}$$

where c_1 is the shear modulus and λ_1 is the principal stretch in all directions based on the isotropy assumption. Accordingly, the nominal stress, σ_1, of the Neo-Hookean model is expressed by

$$\sigma_1 = 2c_1(\lambda_1 - \lambda_1^{-2}) \tag{2}$$

Alternatively, the Ogden material model expresses the strain energy density in terms of a linear combination of principal stretches.[48] Here, the strain energy density and nominal stress for a material under uniaxial tension are

$$W(\lambda_1) = \sum_{i=1}^{m} \frac{\mu_i}{\alpha_i}(\lambda_1^{\alpha_i} + 2\lambda_1^{(-1/2)\alpha_i} - 3) \tag{3}$$

$$\sigma_1 = \sum_{i=1}^{m} \mu_i(\lambda_1^{\alpha_i - 1} - \lambda_1^{(-1/2)\alpha_i - 1}) \tag{4}$$

where μ_i and α_i are material constants describing shear behavior for the ith term of the strain energy density and the nominal stress. The material constants which were determined for eqs 1 through 4 are listed in Table S5.

We then sought to develop a model that could accurately predict the mechanical behavior of the 3D printed porous materials based on the tensile data for the bulk cured resin. Here, the innumerable pores within these materials would require micro- or nanosized FE meshes on the same scale as the pores, which would unfortunately require excessive time to simulate mechanical testing of each sample. Therefore, representative volume elements (RVEs) for FEA were adopted to effectively describe the macroscopic mechanical behavior of the materials with different levels of porosity. RVEs are volumetric subsections that are repeated across space to approximate the structure of an object. The RVEs used in the present study were cubes with unit length having a single spherical void at the cube center, and the void radius was varied to realize the different vol % porosity. Figure 6B shows two representative RVEs for closed- and open-cell materials and their behavior under simulated tension. Other RVEs of porous materials are shown in Figure S19. RVEs above 52.4 vol % were modeled as open-cell because the spherical voids were large enough to contact one another, thus forming open cells across multiple RVEs.

Regardless of porosity level, the performance of the FEA models was found to be strain dependent as demonstrated by the experimental and simulated stress−strain curves for the 33 and 73 vol % porosity samples in Figure 6C. At low strain values (<30%), the stresses calculated using either the Neo-Hookean or Ogden model are similar and close to the experimental values; however, at higher strain rates the calculated stresses deviate slightly from the experimental values. This can be attributed to the fracture of the bulk resin tensile samples at approximately 30% strain. Thus, all FEA-simulated data above 30% strain is entirely predictive without experimental data input from the bulk resin.

Generally, the predicted Neo-Hookean and Ogden model results shown in Figure S20 are in good agreement with the experimental results except for the sample with 53 vol %

https://doi.org/10.1021/acsmaterialsau.1c00017
ACS Mater. Au 2021, 1, 69−80

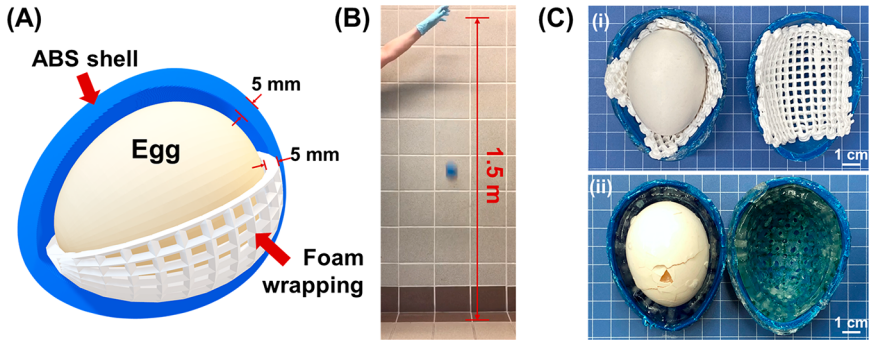

Figure 7. (A) Illustration of the egg container composed of an ABS shell and egg wrapped in lattice prepared by 3DP. (B) Photograph of the egg drop challenge. (C) Photographs of samples after the egg drop experiment: (i) the egg wrapped with 3D printed porous material and (ii) the egg wrapped with pure resin.

porosity, for which the FEA simulation predicted lower stress at each strain value than the experimental result (Figure S20D). This discrepancy is attributed to the assumption that the pores in the FEA simulated materials were of uniform size. In reality, the paraffin beads used as sacrificial filler have a size distribution rather than a single size (Figure S3), and the 53 vol % porosity sample was near this closed-cell/open-cell threshold (52.4 vol %) as observed in the SEM images (Figure S17). Therefore, the experimental porous material likely had a higher volume of closed-cell pores than the simulated material, which had only open-cell pores, as shown by the example RVE cross sections in Figure S21. This caused the FEA simulation to predict lower stresses at 53 vol % than were observed through the experiment.

The Ogden and Neo-Hookean models differed in performance across porosity levels. The normalized root-mean-square errors (RMSEs) of each model at different porosity levels are plotted in Figure 6D. The test data were represented by the stress values at every 5% strain, and the RMSE was normalized by the sampled maximum stress. Below 50 vol % porosity, the RMSE values of the Neo-Hookean model are lower than those of the Ogden model, while at higher porosity (>60 vol %), both models exhibit similar RMSE values. This implies the Neo-Hookean model is more appropriate to represent a 3D porous material at lower porosity levels (i.e., primarily closed-cell pores), whereas the Neo-Hookean and Ogden models are both appropriate for higher porosity levels (i.e., primarily open-cell pores). However, at approximately 53 vol % porosity, both of these models give high RMSE values. This finding aligns with our observations regarding the porosity at which the sample transitions from closed- to open-cell structures.

Current state-of-the-art applications for 3D printed porous materials include a variety of custom materials that absorb the shock of impact, such as shoe midsoles and football helmet linings. To evaluate the impact protection capabilities of our porous structures, a helmet analogue with a soft inner layer made from two cubic lattices of the 63 vol % porosity material was made to protect a raw egg from dropping from a height of 1.5 m (Figure 7). A control protection device was prepared in which the inner layer was made from cured pure resin with holes drilled in it to simulate the macroscale porosity of the printed cubic lattices. The results of the two egg drop tests are displayed in Figure 7C. The egg which was protected by our material did not break, whereas the egg in the control experiment shattered. The microscale porosity within our 3D printed porous materials provides excellent shock absorption capabilities compared to the bulk cured resin with only macroscale porosity. These materials can be 3D printed on demand using readily available components, and the mechanical properties can be tuned based on ink formulation. Further, multiple inks can be combined in the same printed object, allowing for gradients or discrete regions having different mechanical performance. Our 3D printed porous materials from photopolymer/sacrificial paraffin filler have potential uses in both sudden impact protection and longer-term vibration damping applications. Examples include sports helmet linings, packaging for sensitive shipments, and vibration isolation mounts for electronic devices, all of which could have tailor-made geometries through 3D printing.

CONCLUSIONS

In summary, we have reported the facile fabrication of customizable thermoset porous materials via 3D printing and established the structure-processing-property relationships using rheometry, imaging, mechanical testing, and finite element analysis (FEA) simulations. Paraffin particles were leveraged as rheology modifiers to make commercial photopolymer resin thixotropic and printable by DIW. Inks with between 40 and 70 wt % paraffin were found to be printable with different nozzle diameters, thus leading to different resolutions of the printed objects. The depth of cure (DOC) of UV light decreased with increased paraffin loading and leveled out above 40 wt % paraffin, which dictates the filament diameters that can be successfully printed and cured. Paraffin particles were easily removable from printed objects using an organic solvent, leaving micrometer-sized spherical voids dispersed throughout the cured polymer matrix. Modifying the paraffin loading supported that the mechanical properties of the porous material can be tuned: increased paraffin loading resulted in increased compressibility, increased extensibility, and decreased tensile modulus. The porous materials were found to be primarily closed-cell below 53 vol % porosity and primarily open-cell above 53 vol % porosity. Two hyperelastic material models were used to evaluate the effect of porosity on mechanical performance, and the normalized root-mean-square errors of each revealed that the Neo-Hookean model is more appropriate to represent 3D porous materials at all void fractions, while both models are suitable for materials with higher void fractions. Such models can be used to predict the mechanical performance of porous materials.

The present work provides a foundation to better understand and control the mechanical properties of 3D printed objects. For example, by printing with different inks, gradients or regions of varying porosity can be integrated in the same

https://doi.org/10.1021/acsmaterialsau.1c00017
ACS Mater. Au 2021, 1, 69−80

object for use in shoe midsoles and helmet linings with custom stiffness, or porosity zones for selective loading of active materials for controlled release. In future studies, specified pore sizes will be achievable with this system to further tune 3D printed porous materials,[50] and surface area could be optimized by modifying the print path and material porosity to achieve desired surface activity.[51] Our ongoing research focuses on the influence of 3D printing techniques on mechanical properties, along with enhancing the accuracy of the FEA models by simulating pores of varying sizes and shapes. Looking forward, the ability to selectively control the porosity and mechanical properties within flexible components also has applications in soft robotics, where solid photopolymer inks could be used to 3D print structural support materials around electronic devices, and flexible components could be printed and made porous using our reported process. This paves the way to more complex biomimicking soft robots. As 3D printing becomes more widely used to manufacture objects with complicated geometries, the structure−processing−property relationships of 3D printed porous materials form a framework for developing custom printed parts with desired porosity and mechanical performance.

EXPERIMENTAL SECTION

Materials

Photocurable elastic resin was ordered from Formlabs. DecorRom hard resin was ordered from Amazon. Acrylonitrile butadiene styrene (ABS) was obtained from Hyrel. Paraffin wax, Span 20, and ethyl acetate were ordered from Sigma-Aldrich. All chemicals were used as received.

Instrumentation

Optical microscopy images were taken using an AmScope 150C-2L microscope with an 18 MP USB 3.0 camera. The size distribution of paraffin beads was measured with a HORIBA Partica LA-960 particle size distribution analyzer equipped with a fraction cell. Scanning electron microscopy (SEM) images were taken with a TESCAN VEGA SEM. Rheological properties were analyzed using an Anton Parr MCR 302 rheometer with a 25 mm parallel plate. The 3D printing was performed on a Hyrel 3D Engine SR with an SDS-10 syringe extrusion head. Tensile stress−strain profiles were collected on an Instron 5943 Universal Testing System with a 1 kN load cell. Optical images of the printed inks and printed objects were recorded using an iPhone X. Finite element analysis was performed with an implicit solver of Abaqus 2017.

Preparation of Paraffin Beads

A 0.5 mL aliquot of Span 20 was dissolved in water (800 mL), and paraffin wax pellets (50 g) were added. The resulting mixture was heated to 80 °C to melt the paraffin. A high-shear emulsifier, set at 6000 rpm for 3 min, was used to form a paraffin-in-water emulsion. When the emulsion returned to room temperature, solid, spherical paraffin beads were collected by gravity filtration and washed with methanol. The paraffin beads were dried under vacuum at room temperature overnight.

Ink Preparation, 3D Printing, and Paraffin Extraction

In a 20 mL scintillation vial wrapped with aluminum foil, dry paraffin beads were added to photocurable resin at the desired weight percentages. Five photocurable resins (Adaptive3D ToughRubber, DecorRom Hard, Formlabs Elastic, Monocure 3D FLEX100, and SirayaTech Tenacious) were screened for ink formulation, and Formlabs Elastic resin was ultimately selected as it provided optimal rheological performance for printing. The mixture was thoroughly homogenized and loaded into a 5 mL syringe for 3D printing. To print the inks, each ink was charged into a 10 mL Luer-Lok syringe equipped with a blunt dispensing needle (14, 18, and 22 gauge). The loaded syringes were then placed on the extrusion cartridge of the 3D printer, and objects were printed onto a glass bed with a fixed layer height of 0.8, 0.35, and 0.25 mm, infill speed of 5 mm/s, infill of 40%, and cross-linked via *in situ* 365 nm UV exposure after each layer. The printing parameters adopted for the DIW process are summarized in Table 1. Paraffin was extracted from cured paraffin/photopolymer composites by repeated washing with ethyl acetate at 85 °C until all paraffin beads were removed. The porous samples were allowed to return to room temperature in ethyl acetate, then were washed with acetone 3 times, then water 3 times, and freeze-dried to remove water. The removal of paraffin was quantified by measuring the true mass of paraffin beads and elastic resin used to produce a 60 wt % paraffin ink. Three 1 g samples of this ink were cured, then washed to remove paraffin, vacuum-dried, and weighed to determine the mass of paraffin which was removed.

Table 1. DIW Printing Parameters Used with 18G Nozzle

parameters	value	unit
nozzle temperature	25	°C
18G nozzle inner diameter	0.838	mm
layer height	0.35	mm
first layer height	0.35	mm
number of vertical shells	0	
number of horizontal shells	0	
infill density	40%	
infill pattern	rectilinear	
infill speed	5	mm/s
first layer speed	5	mm/s
travel speed	20	mm/s

Depth of Cure Measurements

A 1.5 mL sampling of ink was added to a 2 mL vial and then centrifuged to degas. The vial was centered 5 cm above the 365 nm UV pen of the 3D printer and irradiated at 100% intensity for 60 s. This procedure was repeated for three samples of each ink. The UV pen array was allowed to cool to room temperature between each sample, and samples were cured in random order. The cured samples were retrieved and cut in half vertically. The depth of cure was measured as the height at the midpoint of the cured sample using calipers. The time-dependent experiment was prepared using the same procedure described above with 60 wt % paraffin ink. The samples were exposed to 365 nm light for either 30, 60, 90, 120, 150, or 180 s.

Rheometry

All rheological experiments were performed using an Anton Parr MCR 302 rheometer with a 25 mm parallel plate at 25 °C, with a gap distance of 1 mm. The viscosity of each ink was measured three times over shear rates from 0.01 to 1000 Hz. A stress amplitude sweep was performed on each ink three times from 0.01 to 1000 Pa at a frequency of 1 Hz, and storage and loss moduli were measured.

Tensile Testing

Tensile samples of the resin and inks were cast in molds according to ASTM D412 Type C specifications and cured by 365 nm light. Tensile bars were washed repeatedly with ethyl acetate at 85 °C until all paraffin beads were removed, then washed three times with acetone and three times with water, then dried with a freeze-dryer. The resin tensile bar was also washed and dried under the same conditions. Stress−strain profiles were collected on an Instron 5943 Universal Testing System with a 1 kN load cell at a displacement rate of 20 mm/min.

FEA Simulation of Uniaxial Tensile Tests

Five uniaxial tensile tests were performed as previously described to characterize the deformation behavior of the bulk photopolymer resin. The Neo-Hookean model and the two-term strain energy density (m = 2) of the Ogden model were each used to approximate a tensile test.

https://doi.org/10.1021/acsmaterialsau.1c00017
ACS Mater. Au 2021, 1, 69−80

An implicit solver of Abaqus 2017 was used for the simulations, and a bulk material was meshed with the C3D8RH, 8-node linear hybrid brick element. Loading of an ASTM D412 Type C tensile sample of the bulk resin was applied at a velocity of 20 mm/min. Material constants in eqs 1 through 4 were obtained and are listed in Table S5. The representative volume elements (RVEs) for the porous materials were cubes with unit length and a single spherical void at the cube center, and the void radius was varied on the basis of the desired vol % porosity. To simulate the experimental tensile tests, the bulk porous materials resulting from the removal of the paraffin wax were considered as a set of periodically arranged RVEs comprising the structure of an ASTM D412 Type C tensile sample. The porous materials were meshed with the C3D4H, 4-node linear hybrid tetrahedron element. Loading was applied at a velocity of 20 mm/min.

Egg Drop

A raw egg was measured using calipers, and a 3D model of a 5 mm thick protective case was designed to accommodate 5 mm of space between the egg and the interior of the case. Two halves of the protective case were 3D printed using acrylonitrile butadiene styrene (ABS) filament. Two 7 cm × 7 cm cubic lattices were printed using 60 wt % paraffin ink as previously described, and the paraffin was removed to produce cubic lattices with 63 vol % porosity at the filament level. The cubic lattices were wrapped around the raw egg, which was placed inside the ABS protective case. The two components of the case were joined using DecorRom Hard photopolymer resin, which was cured using a 365 nm UV pen. The protective case containing the egg was dropped from a height of 1.5 m, and the egg was retrieved by separating the two halves of the ABS case. The egg was visually evaluated for any fractures. A lining of bulk Formlabs Elastic resin was prepared for the control experiment by curing a layer of resin at the bottom of a half of the ABS case, then placing the raw egg in the case, adding a small volume of resin, then curing, and repeating this until the space between the egg and the ABS case was filled. This was repeated with the second half of the ABS case. Holes 3 mm in diameter were drilled in this resin lining to simulate the macroscale porosity of the cubic lattices. The control experiment was performed by placing the egg within the two halves of the cured resin lining, then placing the ABS case around them and joining the two halves using DecorRom Hard resin. This case was also dropped from 1.5 m, and the egg was evaluated for fractures as above.

■ ASSOCIATED CONTENT

Supporting Information

The Supporting Information is available free of charge at https://pubs.acs.org/doi/10.1021/acsmaterialsau.1c00017.

> Average depth of cure of each ink after exposure to UV light for 1 minute; average DOCs of 60 wt% paraffin ink at different exposure times; weight of samples of 60 wt% paraffin ink before and after removal of paraffin; paraffin wax loading; material constants used in the Neo-Hookean and Ogden models; finite element analysis methodology; additional figures as described in the text (PDF)

■ AUTHOR INFORMATION

Corresponding Authors

Jyhwen Wang − *Department of Mechanical Engineering and Department of Engineering Technology and Industrial Distribution, Texas A&M University, College Station, Texas 77843, United States*; Email: jwang@tamu.edu

Emily B. Pentzer − *Department of Materials Science and Engineering, Texas A&M University, College Station, Texas 77845, United States; Department of Chemistry, Texas A&M University, College Station, Texas 77843, United States*; orcid.org/0000-0001-6187-6135; Email: emilypentzer@tamu.edu

Peiran Wei − *Department of Materials Science and Engineering, Texas A&M University, College Station, Texas 77845, United States*; Email: peiran@tamu.edu

Authors

Ciera E. Cipriani − *Department of Materials Science and Engineering, Texas A&M University, College Station, Texas 77845, United States*

Taekwang Ha − *Department of Multidisciplinary Engineering, Texas A&M University, College Station, Texas 77843, United States; Department of Mechanical and Industrial Engineering, Norwegian University of Science and Technology, NO-7491 Trondheim, Norway*

Oliver B. Martinez Defilló − *Department of Materials Science and Engineering, Texas A&M University, College Station, Texas 77845, United States*

Manoj Myneni − *Department of Mechanical Engineering, Texas A&M University, College Station, Texas 77843, United States*

Yifei Wang − *Department of Materials Science and Engineering, Texas A&M University, College Station, Texas 77845, United States*

Chandler C. Benjamin − *Department of Mechanical Engineering, Texas A&M University, College Station, Texas 77843, United States*

Complete contact information is available at: https://pubs.acs.org/10.1021/acsmaterialsau.1c00017

Author Contributions

P.W. conceived the research. P.W. developed the resin/paraffin beads ink, 3D printing, and postprocessing methodology. C.C. and O.M. manufactured paraffin beads, inks, tensile test specimens, and performed the mechanical tests, penetration depth experiments, and egg-drop experiments, and P.W. supervised. C.C. and M.M. performed the rheology experiments, and C.B. supervised. C.C. and P.W. performed the confocal microscopy experiments. Y.W. conducted the SEM experiments. P.W. and C.C. analyzed experimental data and interpreted results. T.H. performed the FEA simulations and interpreted the results, and J.W. supervised these simulations. P.W. made all figures. P.W., C.C., and T.H. prepared the original draft, and all the authors reviewed and edited it. E.P. supervised, administrated, and acquired funding for the research.

Notes

The authors declare no competing financial interest.

■ ACKNOWLEDGMENTS

The authors would like to thank Justin Smolen for assisting in the collection of confocal microscope images. Dr. Matt Pharr and Cole Fincher are acknowledged for assisting with tensile testing. This work was funded by NSF DMR CAREER award #1955170 and Texas A&M. Ciera is supported by a NASA Space Technology Graduate Research Opportunity. Peiran would like to thank Bella for his accompany from September 2020 to March 2021.

REFERENCES

(1) Notario, B.; Pinto, J.; Rodriguez-Perez, M. A. Nanoporous Polymeric Materials: A New Class of Materials with Enhanced Properties. *Prog. Mater. Sci.* **2016**, *78*−*79*, 93−139.

(2) Mohammed, A. K.; Usgaonkar, S.; Kanheerampockil, F.; Karak, S.; Halder, A.; Tharkar, M.; Addicoat, M.; Ajithkumar, T. G.; Banerjee, R. Connecting Microscopic Structures, Mesoscale Assemblies, and Macroscopic Architectures in 3D-Printed Hierarchical Porous Covalent Organic Framework Foams. *J. Am. Chem. Soc.* **2020**, *142* (18), 8252−8261.

(3) Mohamed, M. G.; Tsai, M. Y.; Wang, C. F.; Huang, C. F.; Danko, M.; Dai, L.; Chen, T.; Kuo, S. W. Multifunctional Polyhedral Oligomeric Silsesquioxane (POSS) Based Hybrid Porous Materials for CO2 Uptake and Iodine Adsorption. *Polymers* **2021**, *13* (2), 1−15.

(4) Zhang, X.; Wang, B.; Qin, X.; Ye, S.; Shi, Y.; Feng, Y.; Han, W.; Liu, C.; Shen, C. Cellulose Acetate Monolith with Hierarchical Micro/Nano-Porous Structure Showing Superior Hydrophobicity for Oil/Water Separation. *Carbohydr. Polym.* **2020**, *241*, 116361.

(5) Huang, Y.; Gancheva, T.; Favis, B. D.; Abidli, A.; Wang, J.; Park, C. B. Hydrophobic Porous Polypropylene with Hierarchical Structures for Ultrafast and Highly Selective Oil/Water Separation. *ACS Appl. Mater. Interfaces* **2021**, *13* (14), 16859−16868.

(6) Yi, P.; Hu, H.; Sui, W.; Zhang, H.; Lin, Y.; Li, G. Thermoresponsive Polyurethane Sponges with Temperature-Controlled Superwettability for Oil/Water Separation. *ACS Appl. Polym. Mater.* **2020**, *2* (5), 1764−1772.

(7) Shen, X.; Zheng, L.; Tang, R.; Nie, K.; Wang, Z.; Jin, C.; Sun, Q. Double-Network Hierarchical-Porous Piezoresistive Nanocomposite Hydrogel Sensors Based on Compressive Cellulosic Hydrogels Deposited with Silver Nanoparticles. *ACS Sustainable Chem. Eng.* **2020**, *8* (19), 7480−7488.

(8) Wei, P.; Leng, H.; Chen, Q.; Advincula, R. C.; Pentzer, E. B. Reprocessable 3D-Printed Conductive Elastomeric Composite Foams for Strain and Gas Sensing. *ACS Appl. Polym. Mater.* **2019**, *1* (4), 885−892.

(9) Tan, L.; Tan, B. Functionalized Hierarchical Porous Polymeric Monoliths as Versatile Platforms to Support Uniform and Ultrafine Metal Nanoparticles for Heterogeneous Catalysis. *Chem. Eng. J.* **2020**, *390*, 124485.

(10) Tantisriyanurak, S.; Duguid, H. N.; Peattie, L.; Dawson, R. Acid Functionalized Conjugated Microporous Polymers as a Reusable Catalyst for Biodiesel Production. *ACS Appl. Polym. Mater.* **2020**, *2* (9), 3908−3915.

(11) Senatov, F. S.; Niaza, K. V.; Zadorozhnyy, M. Y.; Maksimkin, A. V.; Kaloshkin, S. D.; Estrin, Y. Z. Mechanical Properties and Shape Memory Effect of 3D-Printed PLA-Based Porous Scaffolds. *J. Mech. Behav. Biomed. Mater.* **2016**, *57*, 139−148.

(12) Lee, J. E.; Park, S. J.; Yoon, Y.; Son, Y.; Park, S. H. Fabrication of 3D Freeform Porous Tubular Constructs with Mechanical Flexibility Mimicking That of Soft Vascular Tissue. *J. Mech. Behav. Biomed. Mater.* **2019**, *91*, 193−201.

(13) Petrochenko, P. E.; Torgersen, J.; Gruber, P.; Hicks, L. A.; Zheng, J.; Kumar, G.; Narayan, R. J.; Goering, P. L.; Liska, R.; Stampfl, J.; et al. Laser 3D Printing with Sub-Microscale Resolution of Porous Elastomeric Scaffolds for Supporting Human Bone Stem Cells. *Adv. Healthcare Mater.* **2015**, *4* (5), 739−747.

(14) The Perfect Fit: Carbon + Adidas Collaborate to Upend Athletic Footwear. https://www.carbon3d.com/resources/whitepaper/adidas/ (accessed 2021-03-15).

(15) Leading the Future of Performance Products with Customized Manufacturing. https://formlabs.com/customer-stories/newbalance/ (accessed 2021-03-15).

(16) Riddell Partners with Carbon to Produce First-Ever 3D Printed Football Helmet Liner. https://www.carbon3d.com/news/press-releases/riddell-carbon-produce-football-helmet/ (accessed 2021-05-05).

(17) Lacey, S. D.; Kirsch, D. J.; Li, Y.; Morgenstern, J. T.; Zarket, B. C.; Yao, Y.; Dai, J.; Garcia, L. Q.; Liu, B.; Gao, T.; et al. Extrusion-Based 3D Printing of Hierarchically Porous Advanced Battery Electrodes. *Adv. Mater.* **2018**, *30* (12), 1705651.

(18) Song, P.; Zhou, C.; Fan, H.; Zhang, B.; Pei, X.; Fan, Y.; Jiang, Q.; Bao, R.; Yang, Q.; Dong, Z.; et al. Novel 3D Porous Biocomposite Scaffolds Fabricated by Fused Deposition Modeling and Gas Foaming Combined Technology. *Composites, Part B* **2018**, *152* (May), 151−159.

(19) Lai, J.; Ye, X.; Liu, J.; Wang, C.; Li, J.; Wang, X.; Ma, M.; Wang, M. 4D Printing of Highly Printable and Shape Morphing Hydrogels Consisted of Alginate and Methylcellulose. *Mater. Des.* **2021**, *205*, 109699.

(20) Mishra, A. K.; Wallin, T. J.; Pan, W.; Xu, P.; Wang, K.; Giannelis, E. P.; Mazzolai, B.; Shepherd, R. F. Autonomic Perspiration in 3D-Printed Hydrogel Actuators. *Sci. Robot.* **2020**, *5* (38), eaaz3918.

(21) Piazzoni, M.; Piccoli, E.; Migliorini, L.; Milana, E.; Iberite, F.; Vannozzi, L.; Ricotti, L.; Gerges, I.; Milani, P.; Marano, C.; et al. Monolithic Three-Dimensional Functionally Graded Hydrogels for Bioinspired Soft Robots Fabrication. *Soft Robot.* **2021**, DOI: 10.1089/soro.2020.0137.

(22) Lewis, J. A. Direct Ink Writing of 3D Functional Materials. *Adv. Funct. Mater.* **2006**, *16* (17), 2193−2204.

(23) Larson, R. G.; Wei, Y. A Review of Thixotropy and Its Rheological Modeling. *J. Rheol.* **2019**, *63* (3), 477−501.

(24) Xie, B.; Parkhill, R. L.; Warren, W. L.; Smay, J. E. Direct Writing of Three-Dimensional Polymer Scaffolds Using Colloidal Gels. *Adv. Funct. Mater.* **2006**, *16* (13), 1685−1693.

(25) Smay, J. E.; Cesarano, J.; Lewis, J. A. Colloidal Inks for Directed Assembly of 3-D Periodic Structures. *Langmuir* **2002**, *18* (14), 5429−5437.

(26) Sommer, M. R.; Alison, L.; Minas, C.; Tervoort, E.; Rühs, P. A.; Studart, A. R. 3D Printing of Concentrated Emulsions into Multiphase Biocompatible Soft Materials. *Soft Matter* **2017**, *13* (9), 1794−1803.

(27) Guo, Y.; Liu, Y.; Liu, J.; Zhao, J.; Zhang, H.; Zhang, Z. Shape Memory Epoxy Composites with High Mechanical Performance Manufactured by Multi-Material Direct Ink Writing. *Composites, Part A* **2020**, *135*, 105903.

(28) Minas, C.; Carnelli, D.; Tervoort, E.; Studart, A. R. 3D Printing of Emulsions and Foams into Hierarchical Porous Ceramics. *Adv. Mater.* **2016**, *28* (45), 9993−9999.

(29) Lewis, J. A.; Smay, J. E.; Stuecker, J.; Cesarano, J. Direct Ink Writing of Three-Dimensional Ceramic Structures. *J. Am. Ceram. Soc.* **2006**, *89* (12), 3599−3609.

(30) Weiß, M.; Sälzler, P.; Willenbacher, N.; Koos, E. 3D-Printed Lightweight Ceramics Using Capillary Suspensions with Incorporated Nanoparticles. *J. Eur. Ceram. Soc.* **2020**, *40* (8), 3140−3147.

(31) Chen, Q.; Cao, P.; Advincula, R. C. Mechanically Robust, Ultraelastic Hierarchical Foam with Tunable Properties via 3D Printing. *Adv. Funct. Mater.* **2018**, *28* (21), 1800631.

(32) Wei, P.; Cipriani, C. E.; Pentzer, E. B. Thermal Energy Regulation with 3D Printed Polymer-Phase Change Material Composites. *Matter* **2021**, *4* (6), 1975−1989.

(33) Mu, X.; Bertron, T.; Dunn, C.; Qiao, H.; Wu, J.; Zhao, Z.; Saldana, C.; Qi, H. J. Porous Polymeric Materials by 3D Printing of Photocurable Resin. *Mater. Horiz.* **2017**, *4* (3), 442−449.

(34) Cooperstein, I.; Layani, M.; Magdassi, S. 3D Printing of Porous Structures by UV-Curable O/W Emulsion for Fabrication of Conductive Objects. *J. Mater. Chem. C* **2015**, *3* (9), 2040−2044.

(35) Karyappa, R.; Ohno, A.; Hashimoto, M. Immersion Precipitation 3D Printing (Ip3DP). *Mater. Horiz.* **2019**, *6*, 1834.

(36) Dong, Z.; Cui, H.; Zhang, H.; Wang, F.; Zhan, X.; Mayer, F.; Nestler, B.; Wegener, M.; Levkin, P. A. 3D Printing of Inherently Nanoporous Polymers via Polymerization-Induced Phase Separation. *Nat. Commun.* **2021**, *12* (1), 247.

(37) Alison, L.; Menasce, S.; Bouville, F.; Tervoort, E.; Mattich, I.; Ofner, A.; Studart, A. R. 3D Printing of Sacrificial Templates into Hierarchical Porous Materials. *Sci. Rep.* **2019**, *9* (1), 1−9.

(38) Mayer, F.; Ryklin, D.; Wacker, I.; Curticean, R.; Čalkovský, M.; Niemeyer, A.; Dong, Z.; Levkin, P. A.; Gerthsen, D.; Schröder, R. R.;

https://doi.org/10.1021/acsmaterialsau.1c00017
ACS Mater. Au 2021, 1, 69−80

et al. 3D Two-Photon Microprinting of Nanoporous Architectures. *Adv. Mater.* **2020**, *32*, 1−7.
(39) Shen, J. W.; Matsumoto, H.; Maki, A.; Kuriyama, T.; Nemoto, T.; Koido, S.; Takeuchi, H. A Study on the Relationship between Microstructure and Mechanical Properties of Porous Polymer Films. *Polymer* **2020**, *204*, 122784.
(40) Maheo, L.; Viot, P.; Bernard, D.; Chirazi, A.; Ceglia, G.; Schmitt, V.; Mondain-Monval, O. Elastic Behavior of Multi-Scale, Open-Cell Foams. *Composites, Part B* **2013**, *44* (1), 172−183.
(41) Petit, C.; Meille, S.; Maire, E. Cellular Solids Studied by X-Ray Tomography and Finite Element Modeling - A Review. *J. Mater. Res.* **2013**, *28* (17), 2191−2201.
(42) Donley, G. J.; Singh, P. K.; Shetty, A.; Rogers, S. A. Elucidating the G″ Overshoot in Soft Materials with a Yield Transition via a Time-Resolved Experimental Strain Decomposition. *Proc. Natl. Acad. Sci. U. S. A.* **2020**, *117* (36), 21945−21952.
(43) Dinkgreve, M.; Paredes, J.; Denn, M. M.; Bonn, D. On Different Ways of Measuring "the" Yield. *J. Non-Newtonian Fluid Mech.* **2016**, *238*, 233−241.
(44) Zhao, D.; Ge, S.; Senses, E.; Akcora, P.; Jestin, J.; Kumar, S. K. Role of Filler Shape and Connectivity on the Viscoelastic Behavior in Polymer Nanocomposites. *Macromolecules* **2015**, *48* (15), 5433−5438.
(45) Xiang, Y.; Schilling, C.; Arora, N.; Boydston, A. J.; Rudykh, S. Mechanical Characterization and Constitutive Modeling of Visco-Hyperelasticity of Photocured Polymers. *Addit. Manuf.* **2020**, *36*, 101511.
(46) Rivlin, R. S. Large Elastic Deformations of Isotropic Materials. *Philos. Trans. R. Soc. London. Ser. A, Math. Phys. Sci.* **1948**, *241*, 379−397.
(47) Mooney, M. A Theory of Large Elastic Deformation. *J. Appl. Phys.* **1940**, *11* (9), 582−592.
(48) Ogden, R. W. Large Deformation Isotropic Elasticity−on the Correlation of Theory and Experiment for Incompressible Rubberlike Solids. *Proc. R. Soc. London. A. Math. Phys. Sci.* **1972**, *326* (1567), 565−584.
(49) Yeoh, O. H. Some Forms of the Strain Energy Function for Rubber. *Rubber Chem. Technol.* **1993**, *66* (5), 754−771.
(50) Costantini, M.; Jaroszewicz, J.; Kozoń, Ł.; Szlązak, K.; Świeszkowski, W.; Garstecki, P.; Stubenrauch, C.; Barbetta, A.; Guzowski, J. 3D-Printing of Functionally Graded Porous Materials Using On-Demand Reconfigurable Microfluidics. *Angew. Chem., Int. Ed.* **2019**, *58* (23), 7620−7625.
(51) Buj-Corral, I.; Bagheri, A.; Petit-Rojo, O. 3D Printing of Porous Scaffolds with Controlled Porosity and Pore Size Values. *Materials* **2018**, *11* (9), 1532.

https://doi.org/10.1021/acsmaterialsau.1c00017
ACS Mater. Au 2021, 1, 69−80